

# Hydrogen trapping state associated with the low temperature thermal desorption spectroscopy peak in hydrogenated nanostructured graphite

Yumiko Miyabe,<sup>a)</sup> Tomoko Yoshida, Shunsuke Muto, Tetsu Kiyobayashi, and Hiroaki Wasada

*Department of Materials, Physics and Energy Engineering, Graduate School of Engineering, Nagoya University, Chikusa-ku, Nagoya 464-8603, Japan; Research Institute for Ubiquitous Energy Devices, National Institute of Advanced Industrial Science and Technology (AIST), 1-8-13, Midorigaoka, Ikeda, Osaka 563-8577, Japan; and Faculty of Regional Studies, Gifu University, 1-1 Yanagido, Gifu 501-1193, Japan*

(Received 11 February 2008; accepted 6 June 2008; published online 26 August 2008)

Hydrogenated nanostructured graphite has been reported to exhibit a characteristic peak at around 600–800 K in thermal desorption spectroscopy (TDS). The origin of this peak is still controversial. We have reexamined it based on a combination Fourier transform infrared (FT-IR), electron diffraction, and electron energy-loss spectroscopy (EELS) study. The FT-IR spectrum of HNG exhibited an unknown broad absorption band at very low frequencies around 660  $\text{cm}^{-1}$ , which almost disappeared by annealing up to 800 K. Electron diffraction as well as plasmon peaks in EELS detected unusual shrinkage and subsequent expansion of the graphene interlayer distance by hydrogen incorporation and desorption with annealing, which were well correlated with the change in intensity of the 660  $\text{cm}^{-1}$  IR band. An energetically stable configuration was found by theoretical model calculations based on GAUSSIAN03. All the present results are consistent with our previous studies, which suggested that hydrogen is loosely trapped between graphene layers [S. Muto *et al.*, *Jpn. J. Appl. Phys.* **44**, 2061 (2005); T. Kimura *et al.*, *J. Alloys Compd.* **413**, 150 (2006)]. © 2008 American Institute of Physics. [DOI: 10.1063/1.2965192]

## I. INTRODUCTION

For practical hydrogen-storage applications, studies on hydrogen adsorption on the surfaces and interfaces of various materials are of importance. Carbon-related materials have been investigated for hydrogen storage because they are relatively light and inexpensive compared to metallic hydrogen-storage materials. Carbon nanotubes (CNTs) were expected to be a promising hydrogen-storage candidate material.<sup>1,2</sup> However, pure CNTs were found not to be able to stably store hydrogen at ambient temperature and pressure. It is currently known that CNTs physically adsorb hydrogen but only at temperatures lower than 100 K.<sup>3</sup>

It was found that nanostructured graphite prepared by mechanical milling in a hydrogen atmosphere [referred to as hydrogenated nanostructured graphite (HNG) hereafter] showed a high capacity for hydrogen storage, yielding a composition as high as  $\text{CH}_{0.95}$ .<sup>4</sup> The thermal desorption spectrum<sup>5</sup> (TDS) of this sample exhibited a characteristic broad peak between 600 and 800 K, other than higher temperature peaks corresponding to C–H covalent bonding and other bonding states.<sup>5,6</sup> The present authors' group intensively studied this material using electron energy-loss spectroscopy (EELS) and concluded that the broad TDS peak could be attributed to H loosely trapped between defective graphene layers. This conclusion was, however, drawn from indirect evidence, because EELS probes the electronic states

of the carbon matrix, which was modified by H incorporation. This study revisits H corresponding to the broad TDS peak, whose origin is still controversial.

In the present study, we attempted to find a specific local vibrational mode (LVM) corresponding to the hydrogen trapping state between graphene layers by means of Fourier transform infrared (FT-IR) spectroscopy. We also carried out theoretical calculations to confirm whether the observed LVM could be reproduced by our proposed model. Additional experiments using EELS and electron diffraction were also carried out to further reinforce our proposal.

## II. EXPERIMENTAL

Samples were prepared by mechanically milling crystalline graphite in a hydrogen atmosphere of 0.7 MPa for 90 h at 300 rpm in a Cr/Ni steel mortar using a Fritsch *P-6* planetary ball mill. For comparison, samples mechanically milled under the same conditions but in an argon atmosphere were also prepared, hereafter abbreviated as “ANG.” Some of the samples powder were heat treated in a vacuum vessel with a heating rate of 10 K/min. The sample was cooled when the sample temperature reached 650, 800, and 1000 K. The samples for IR measurements were prepared by diluting  $8 \times 10^{-5}$  mol of the sample powder by  $8 \times 10^{-6}$  mol of KBr and molding the mixture into a pellet 10 mm in diameter ( $\sim 1$  mm in thickness). Another portion of the sample powder was dispersed on a ceramic film mesh (DuraSiN™) for annealing experiments in a transmission electron microscope (TEM).

The FT-IR spectra were measured using a JASCO FT/

<sup>a)</sup>Electronic mail: t-yoshida@nucl.nagoya-u.ac.jp.

IR-610 in transmission mode at room temperature. In order to avoid the effects of moisture on air, the FT-IR measurements were carried out in vacuum. Electron diffraction analysis and EELS measurements were performed using a JEM200CX TEM equipped with a Gatan ENFINA 1000 spectrometer. The TEM was operated at 160 kV for EELS and at 200 kV for electron diffraction experiments.

### III. THEORETICAL CALCULATIONS

Energetically possible configurations for the hydrogen-graphene system were sought using the GAUSSIAN03 program package<sup>7</sup> to confirm whether the experimental results are theoretically reproducible by the model structure. In order to take into account weakly trapped hydrogen between graphene layers, the van der Waals interaction between the layers should be included, and we adopted the second order Møller–Plesset (MP2) method<sup>8</sup> for structural optimization and vibrational analysis.

We first prepared two graphene layers, each including 13 carbon atoms with the unsaturated bonds at the edge terminated by hydrogen. The atomic configuration of the two graphene layers was optimized without hydrogen using the 6–31G\*\* basis set to reproduce the van der Waals interaction between the layers by taking electron polarization effects into consideration.<sup>9</sup> We obtained a 2H graphite structure with an average interlayer spacing of 3.40 Å after the optimization, which is in reasonable agreement with the experimental value for graphite of 3.35 Å. Then, a single hydrogen atom was inserted into the middle of the graphene layers, on the line joining the central carbon atom in each layer. Starting from this atomic configuration, the structure was energetically optimized. Since we might seek states of energetically very subtle differences, the following tricks were applied: First, we fixed the C–H–C distance of interest and relaxed the other atoms. After the confined structural optimization, we relaxed all the atoms including the hydrogen atom. The following three cases were considered: The inserted hydrogen was neutral (atomic, H<sup>0</sup>), positively charged (H<sup>+</sup>) or negatively charged (H<sup>-</sup>) as the initial condition, hereby referred to as models A, B, and C, respectively. For model C, the 6–31++G\*\* basis set was adapted to the negatively charged hydrogen to include the extended charge distribution of the extra electron introduced by higher order molecular orbitals.<sup>10</sup>

## IV. RESULTS

### A. FT-IR results

The FT-IR spectra of the HNG samples are shown in Fig. 1. We found groups of absorption bands of (i) 807, 875, 1026, 1090, and 1260 cm<sup>-1</sup>, (ii) 1357, 1453, and 1600 cm<sup>-1</sup>, and (iii) 2855, 2920, and 2953 cm<sup>-1</sup>, which are, respectively, assigned to the bending modes of H bonded to aromatic carbon, olefinic carbon, and stretching modes of H bonded to olefinic carbon, according to the conventional nomenclature.<sup>11–14</sup> The fine absorption peaks observed around 1365–2017 and 2727–3000 cm<sup>-1</sup> are attributable to residual water. They completely disappeared after heating in vacuum to 373 K. In addition to these known bands, an

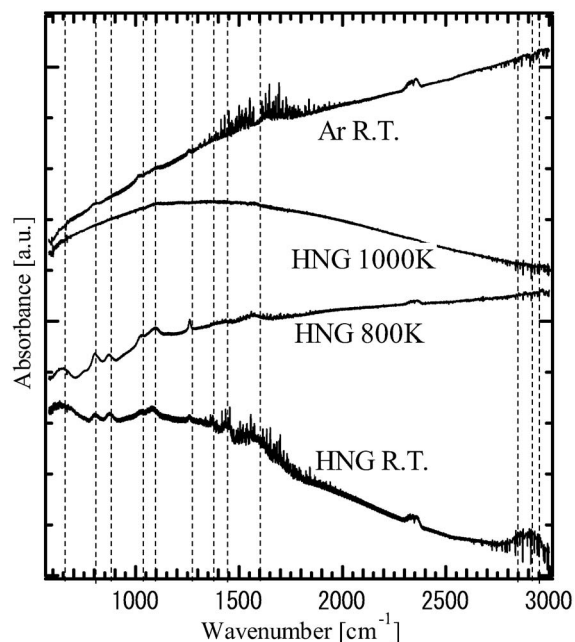


FIG. 1. FT-IR spectra of HNG samples annealed at the indicated temperatures, together with that of ANG for comparison.

unknown characteristic broadband at a very low frequency at around 660 cm<sup>-1</sup> was observed. This broad absorption band was not observed in the ANG sample. After heating to 800 K, the IR bands of group (ii) and (iii) decreased significantly; this corresponds to a release of H in the form of CH<sub>x</sub> molecules according to previous research.<sup>15</sup> The broadband intensity decreased by 80% after the sample was heated to 800 K. By further annealing up to 1000 K, the IR bands of group (i) almost disappeared. These behaviors are well correlated with the first two broad peaks in the TDS result. Hence, the 660 cm<sup>-1</sup> absorption peak corresponds to the lower temperature TDS peak, which could be attributed to a weakly bound hydrogen trapping state.

### B. Electron diffraction patterns

It is known that the interlayer spacing of graphitic basal planes [(002) planes] is increased not only by intercalations of impurities but also by crystal imperfections and fragmentation. The present authors' group has described expansion up to ~11% associated with electron irradiation damage.<sup>16</sup> Hence the interlayer spacing can be used as a degree of lattice imperfection and a measure of average crystallite size.<sup>17</sup> We measured the interlayer spacing of the fragmented graphene sheets using the radius of the 002-electron diffraction ring. A typical electron diffraction pattern of the as-prepared HNG and the line profiles of the patterns from the as-prepared and annealed samples are shown in Fig. 2. The extra peak at 0.58 Å for the sample annealed at 1000 K corresponds to the (110) reflection of Fe<sub>3</sub>C (cementite) contained in the sample as a contaminant derived from the mortar and ball during the mechanical milling.

The changes in the interlayer spacing,  $d_{002}$ , of the HNG and ANG samples are shown in the lower part of Fig. 3 (closed symbols) as functions of the annealing temperature.  $d_{002}$  of ANG slightly but gradually decreased with the an-

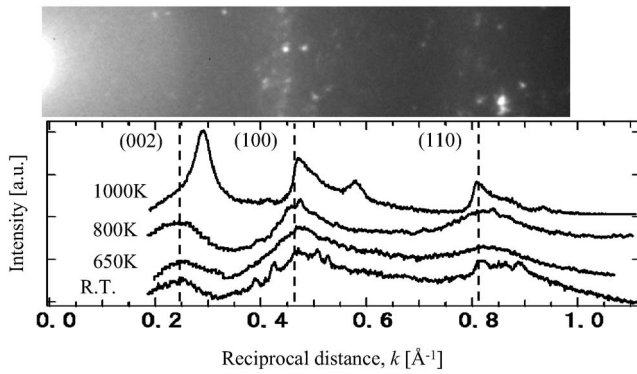


FIG. 2. A representative electron diffraction pattern (upper photo) and the intensity profiles of HNG samples annealed at the indicated temperatures (lower figure).

nealing temperature, corresponding to deintercalation of Ar atoms and thermal structural recovery. On the other hand,  $d_{002}$  of the HNG sample is first increased by 0.2 Å with increasing temperature up to 800 K, followed by a sudden decrease at higher temperatures.

### C. Change in $\pi-\pi^*$ volume plasmon

We measured the  $\pi-\pi^*$  plasmon energy of the samples by TEM-EELS. The EEL spectra in the plasmon loss region are shown in Fig. 4. The  $\pi-\pi^*$  plasmon peak intensity evolved with the annealing temperature, which corresponds to an increase in the coherent length normal to the graphene layer, indicating thermal recovery of the layered structure. The changes in the  $\pi-\pi^*$  plasmon peak position for the HNG and ANG samples as a function of the annealing temperature are also shown in the upper part of Fig. 3 (open symbols). The volume plasmon is defined as collective excitation of the valence electrons, and the  $\pi-\pi^*$  plasmon originates from the  $sp^2-\pi$  bonding (C  $2p_z$  orbitals) of graphite. The plasmon energy  $E_p$  is expressed by the Eq. (1), based on the Drude model,<sup>18</sup>

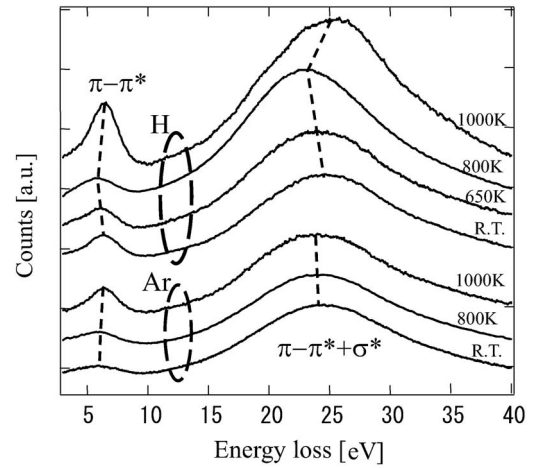


FIG. 4. EELS spectra of the plasmon region for the HNG and ANG samples for different annealing temperatures.

$$E_p = \hbar \sqrt{\frac{ne^2}{\epsilon_0 m}} \propto \sqrt{\frac{N}{V}}, \quad (1)$$

where  $n$  is the density of the valence electrons,  $e$  is the electron charge,  $m$  is the effective electron mass,  $\hbar$  is Planck's constant divided by  $2\pi$ , and  $\epsilon_0$  is the dielectric constant in vacuum. Equation (1) indicates that the plasmon energy is proportional to the square root of the valence electron density. Assuming that the  $\pi^*$ -plasmon is only proportional to the graphene interlayer distance, we can estimate the plasmon energy from the measured interlayer distance, the results of which are also shown in Fig. 3. For the ANG sample, the measured and estimated plasmon energies are consistent with each other within experimental accuracy, confirming the validity of the assumption, while for the HNG sample the measured plasmon energies are significantly larger than those estimated from the interlayer distances before the annealing temperature reaches 800 K. This suggests that the hydrogen trapping state in this temperature range (corresponding to the low temperature peak in TDS) should exhibit an apparent increase in the valence electron density.

All the experimental results above support our hypothesis that the low temperature peak in TDS can be attributed to hydrogen loosely trapped between the graphene layers. In Sec. IV, we discuss this from a theoretical viewpoint and examine whether the deduced model is consistent with the experimental results.

## V. DISCUSSION

### A. Possible C–H configurations by theoretical considerations

The optimized structures for the three initial hydrogen charge states are shown in Figs. 5(a)–5(c), respectively. The resultant distances between the introduced hydrogen atom and its nearest carbon atoms are tabulated in Table I. The models for neutral (model A) and positively charged (model B) hydrogen converged to a very similar structure, wherein the hydrogen forms an  $sp^3$  covalent bond (C–H bond lengths = 1.11–1.18 Å) to the central C atom of either of the graphene sheets, and the H-bonded C atom protrudes from

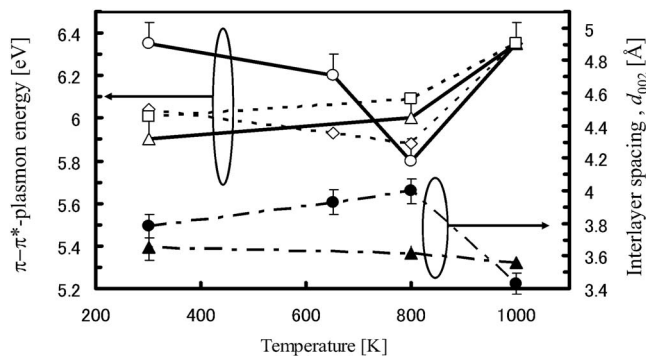


FIG. 3. Changes in  $d_{002}$  spacing (closed symbol) and  $\pi-\pi^*$  plasmon energy  $E_p$  (experimental and calculated, open symbols) of HNG and ANG as functions of the annealing temperature. Open circle:  $E_{p\pi-\pi^*}$  for HNG, open diamond:  $E_{p\pi-\pi^*}$  for HNG (calc.), open triangle:  $E_{p\pi-\pi^*}$  for ANG, open square:  $E_{p\pi-\pi^*}$  for ANG (calc.), closed circle:  $d_{002}$  for HNG, closed triangle:  $d_{002}$  for ANG. See text for detail.

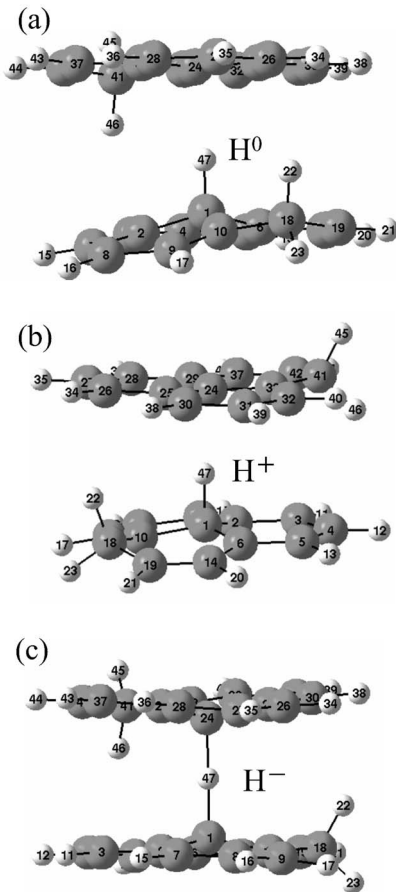


FIG. 5. Model structures containing a hydrogen atom between the two graphene layers for theoretical calculations: (a) Model A: neutral hydrogen atom,  $H^0$  (one proton and one electron), (b) model B: positively charged,  $H^+$  (one proton and no electron), and (c) model C: negatively charged,  $H^-$  (one proton and two electrons) incorporated. The figures are presented as the final optimized structures.

the graphene sheet plane accordingly. Note that the C24–H47 distances (nonbonding) for models A and B are, respectively, 2.42 and 1.91 Å, as shown in Table I. This configuration is consistent with previous local density approximation (LDA) band calculation results.<sup>19,20</sup> On the other hand, for the negatively charged hydrogen (model C), the hydrogen was stabilized halfway between the facing C atoms [C1 and C24 in Fig. 5(c)] at the center of each graphene sheet. The C1–H47 and C24–H47 distances are 1.33 and 1.37 Å, respectively, which are significantly longer than the stable C–H covalent bond length, but significantly shorter than that observed by neutron diffraction (1.8 Å).<sup>21</sup> The graphene sheets are slightly distorted so that C1 and C24 are shifted toward each other, as shown in Fig. 5(c).

Note that the average interlayer distance of model C is the smallest among the three models in which hydrogen is incorporated between the graphene sheets, as shown in Table I. The formation of a strong C–H covalent bond (i.e., models A and B) instead of the loosely bound hydrogen state (model C) further dilates the average interlayer distance, which could be the cause of the significant increase in  $d_{002}$  by annealing at temperatures higher than 800 K, as shown in Sec. IV B.

Although model C [Fig. 5(c)] seems most consistent with the present experimental results, readers may feel reluctant to introduce the negatively charged hydrogen for the initial state. To see where the extra electron is redistributed in the optimized structure, the charge difference between the optimized state and the model of two graphene sheets and a single (neutral) hydrogen atom with the same atomic positions is shown in Fig. 6. The charge is increased between H47–C1 and H47–C24, associated with weak bond formation, and around the peripheral carbon atoms. The population analysis of Mulliken<sup>22</sup> showed that the net charge of the hydrogen atom was increased only by 0.3. However, the majority of electrons introduced were uniformly shared by the carbon atoms in the optimized structure. This means that the negative charge state of hydrogen was only necessary to find an energetically stable state with the hydrogen trapped between the graphene layers, as experimentally expected, as an initial condition within the present computational scheme. The charge state of hydrogen does not matter for the final stable structure, which reasonably models the experimentally found state. We then proceeded further to see whether model C is quantitatively consistent with other experimental results. In the actual experimental situation, the fragmented graphene sheets would be much larger and would easily accommodate such uneven charge distributions to stabilize such a configuration.

In order to discuss the interaction between the graphene layers and hydrogen, we conducted overlap population analysis<sup>22</sup> between C1  $2p_z$  and H47  $1s$  orbitals in models A and C, as shown in Fig. 7, where the highest occupied molecular orbital is set at 0 eV. The primary positive peaks indicate covalent bonding between H and C. The  $-7.1$  eV peak for model A corresponds to strong  $sp^3$ -like hybridization between C1 and H47. On the other hand, model C exhibits a shallow level related to the C–H bond as a sharp peak at  $-0.8$  eV, the corresponding wave function (molecular orbital) of which is shown in Fig. 8(a). The molecular orbital contains 2 electrons, 1.2 net electrons of which occupy the C1–H47 bond ( $2p_z$  of C2 and  $1s$  of H47) and 97%

TABLE I. Calculated interatomic and interlayer distances in units of angstrom for the three model structures after structural optimization.

Model	C1–H47	C24–H47	Average	Layer distance	
				Minimum	Maximum
No H	...	...	3.40	3.35	3.45
Model A ( $H^0$ )	1.11	2.42	3.90	3.20	4.10
Model B ( $H^+$ )	1.18	1.91	3.75	3.00	3.75
Model C ( $H^-$ )	1.33	1.37	3.70	2.70	3.70

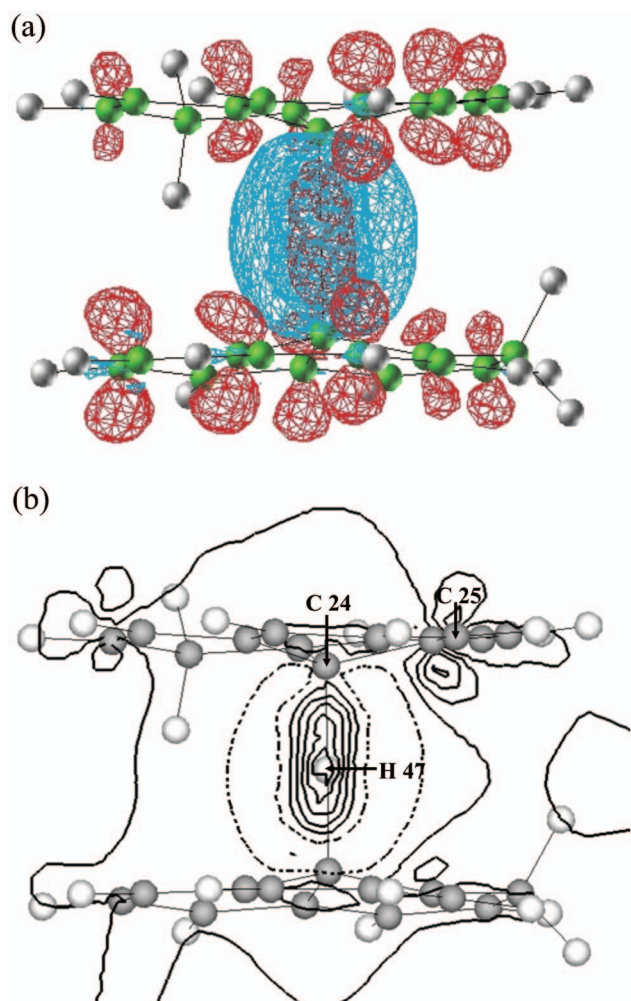


FIG. 6. (Color) Difference in spatial charge distributions between model C (after optimization) and two graphene sheets and a single (neutral) hydrogen atom with the same atomic positions. (a) Three-dimensional surface layer representation at the threshold of 0.005 electrons/Å<sup>3</sup> for electron excess portions (red) and -0.0007 electrons/Å<sup>3</sup> for electron deficient portions (blue). (b) Contour map representation sectioned by the plane containing C24, C25, and H47. The contour line interval is 0.0045 electrons/Å<sup>3</sup>.

are transferred to the H47 side. This suggests that the C–H bond in model C is rather weak and the electron occupancy of the associated  $2p_z$  orbital is reduced, which is consistent with our previous study.<sup>5,6</sup> The amplitudes of the wave functions corresponding to the energy levels of -4.0 eV in model

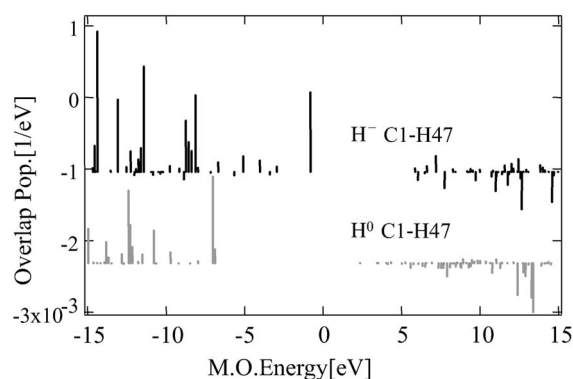


FIG. 7. Overlap populations between C1  $2p_z$  and H47  $1s$  orbitals for models A and C.

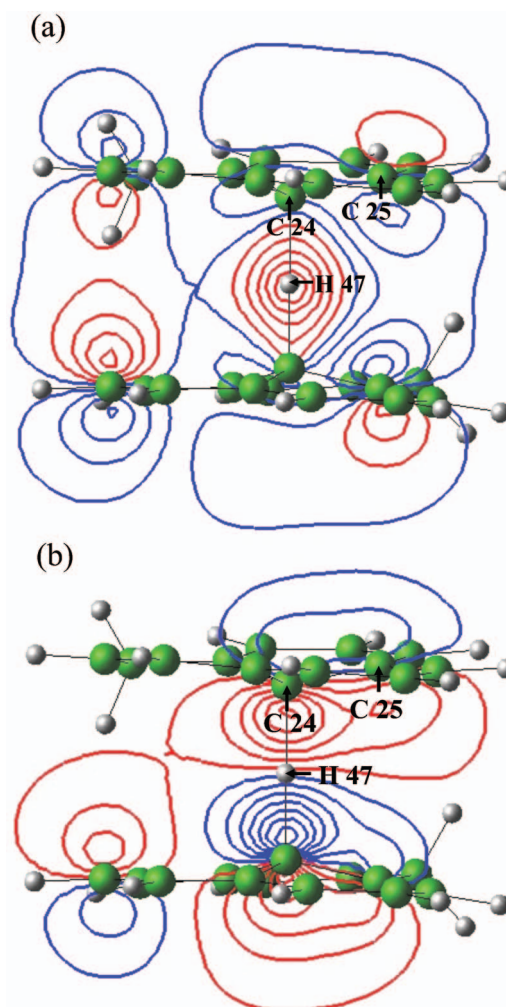


FIG. 8. (Color) Contour map representations of wave functions for molecular orbitals of (a) -0.8 eV and (b) -4.0 eV, sectioned by the plane containing C24, C25, and H47.

C are also visualized in Fig. 8(b) as a contour map sectioned by the plane containing C24, C25, and H47. This clearly shows  $pp\pi$  bonding between C24 and C25, which is unambiguous evidence that the  $sp^2$  bonding is maintained between the carbon atoms.

The binding energy of H47 in model C was estimated to be 0.8 eV (0.63 eV) by subtracting the total energy of model C from that of the two graphene layers and a negatively charged (neutral) hydrogen atom. Diño *et al.*<sup>19</sup> calculated the activation energy of the hydrogen atom trapped between crystalline graphene layers to be 0.3–0.4 eV based on DFT. Our value cannot be directly compared with their value, however, considering that the binding energy of the  $sp^3$  C–H bond is 7–10 eV in the present computational model, it is quite reasonable to assign the low temperature TDS peak to the present C–H–C trapping state.

## B. IR active local modes

Normal vibrational mode analysis was carried out for the optimized structures by means of the MP2 perturbation theory.<sup>8</sup> The IR active modes among the possible LVM are listed in Table II, together with the IR modes experimentally

TABLE II. Experimental IR absorption peak ( $\nu_{\text{expt}}$ , first column) and calculated IR active LVMs [frequencies ( $\nu_{\text{calc}}$ ) and intensities ( $I$ )] for the three model structures. The symbols of the attributions are illustrated in Fig. 9.

HNG sample		Model A ( $H^0$ )			Model B ( $H^+$ )			Model C ( $H^-$ )		
$\nu_{\text{expt}}(\text{cm}^{-1})$	Attribution $\nu(\text{CH})$	$\nu_{\text{calc}}(\text{cm}^{-1})$	$I$	Attribution	$\nu_{\text{calc}}(\text{cm}^{-1})$	$I$	attribution	$\nu_{\text{cal}}(\text{cm}^{-1})$	$I$	attribution $\nu(\text{CH})$
660		704	12.4	$\delta_{\text{op}}(\text{arom CH})$	705	13.2	$\delta_{\text{op}}(\text{arom CH})$	<b>644</b>	<b>249.2</b>	
807	$\delta_{\text{ip}}(\text{arom CH})$	760	124.6	$\delta_{\text{ip}}(\text{arom CH})$	712	49.1	$\delta_{\text{op}}(\text{arom CH})$	792	21.3	$\delta_{\text{ip}}(\text{arom CH})$
875	$\delta_{\text{ip}}(\text{arom CH})$	790	85.2	$\delta_{\text{ip}}(\text{arom CH})$	804	50.6	$\delta_{\text{ip}}(\text{arom CH})$	798	90.4	$\delta_{\text{ip}}(\text{arom CH})$
		880	9.6	$\delta_{\text{ip}}(\text{arom CH})$	811	55.6	$\delta_{\text{ip}}(\text{arom CH})$	801	9.4	$\delta_{\text{ip}}(\text{arom CH})$
					816	71.2	$\delta_{\text{ip}}(\text{arom CH})$	806	8.9	$\delta_{\text{ip}}(\text{arom CH})$
					818	29.2	$\delta_{\text{ip}}(\text{arom CH})$	817	60.6	$\delta_{\text{ip}}(\text{arom CH})$
					854	44.8	$\delta_{\text{ip}}(\text{arom CH})$	867	6.9	$\delta_{\text{ip}}(\text{arom CH})$
1026	$\delta_{\text{op}}(\text{arom CH})$	916	29.0	$\delta_{\text{op}}(\text{arom CH})$	870	8.2	$\delta_{\text{op}}(\text{arom CH})$	944	28.0	$\delta_{\text{op}}(\text{arom CH})$
1090	$\delta_{\text{op}}(\text{arom CH})$	940	20.9	$\delta_{\text{op}}(\text{arom CH})$	1069	8.3	$\delta_{\text{op}}(\text{arom CH})$	1046	11.4	$\delta_{\text{op}}(\text{arom CH})$
1260	$\delta_{\text{op}}(\text{arom CH})$	1085	6.0	$\delta_{\text{op}}(\text{arom CH})$	1212	8.3	$\delta_{\text{op}}(\text{arom CH})$	1083	12.2	$\delta_{\text{op}}(\text{arom CH})$
		1208	7.3	$\delta_{\text{op}}(\text{arom CH})$	1226	7.2	$\delta_{\text{op}}(\text{arom CH})$	1166	10.3	$\delta_{\text{op}}(\text{arom CH})$
		1245	7.1	$\delta_{\text{op}}(\text{arom CH})$				1216	31.3	$\delta_{\text{op}}(\text{arom CH})$
								1236	111.4	$\delta_{\text{op}}(\text{arom CH})$
								1270	30.2	$\delta_{\text{op}}(\text{arom CH}), \nu(\text{CH})$
					1361	34.6	$\delta_{\text{ip}}(\text{arom CH})$	1289	68.3	$\delta_{\text{ip}}(\text{arom CH}), \nu(\text{CH})$
								1362	32.9	$\delta_{\text{ip}}(\text{arom CH}), \nu(\text{CH})$
								1372	25.9	$\delta_{\text{ip}}(\text{arom CH}), \nu(\text{CH})$
1375	$\delta(\text{CH}_3)$	1411	8.5	$\nu(\text{C}=\text{C})$	1397	52.4	$\delta(\text{CH}_2), \nu(\text{C}=\text{C})$	1340	76.9	$\nu(\text{C}=\text{C}), \nu(\text{CH})$
1400–1450	$\delta(\text{CH}_2, \text{CH}_3), \nu(\text{C}=\text{C})$	1489	15.0	$\delta(\text{CH}_2)$	1420	32.0	$\delta(\text{CH}_2), \nu(\text{C}=\text{C})$	1478	10.5	$\nu(\text{C}=\text{C})$
1550–1600	$\delta(\text{CH}_2, \text{CH}_3), \nu(\text{C}=\text{C})$	1490	6.5	$\delta(\text{CH}_2)$	1491	32.4	$\delta(\text{CH}_3)$	1517	104.9	$\nu(\text{C}=\text{C}), \nu(\text{CH})$
		1557	3.2	$\delta(\text{CH}_2), \nu(\text{C}=\text{C})$	1528	34.5	$\delta(\text{CH}_2), \nu(\text{C}=\text{C})$	1538	37.7	$\delta(\text{CH}_2), \nu(\text{C}=\text{C})$
					1551	16.1	$\delta(\text{CH}_2), \nu(\text{C}=\text{C})$	1559	185.0	$\delta(\text{CH}_2), \nu(\text{C}=\text{C})$
					1572	86.6	$\delta(\text{CH}_2), \nu(\text{C}=\text{C})$	1576	15.0	$\delta(\text{CH}_2), \nu(\text{C}=\text{C})$
					1618	23.1	$\nu(\text{C}=\text{C})$	1578	11.1	$\delta(\text{CH}_2), \nu(\text{C}=\text{C})$
					1623	30.8	$\nu(\text{C}=\text{C})$	1632	56.1	$\nu(\text{C}=\text{C})$
					1657	61.3	$\nu(\text{C}=\text{C})$	1638	15.8	$\nu(\text{C}=\text{C})$
								1671	45.9	$\nu(\text{C}=\text{C})$
					2065	2105.4	$\delta(\text{CH})$			
2855	$\nu_{\text{sym}}(\text{CH}_2)$	2881	15.4	$\nu_{\text{sym}}(\text{CH}_2)$				2911	42.3	$\nu_{\text{sym}}(\text{CH}_2)$
2920	$\nu_{\text{asym}}(\text{CH}_2, \text{CH}_3)$	2930	13.2	$\nu_{\text{sym}}(\text{CH}_2)$				2913	30.5	$\nu_{\text{sym}}(\text{CH}_2)$
2953	$\nu_{\text{sym}}(\text{CH}_2)$	2942	15.0	$\nu_{\text{sym}}(\text{CH}_2)$				2944	28.9	$\nu_{\text{sym}}(\text{CH}_2)$

observed in the HNG sample at RT. Dual scaling factors were used to improve the agreement between experimental and theoretical LVM frequencies.<sup>23</sup> The theoretical LVMs are grouped by their frequencies corresponding to the experimentally observed IR bands. The symbols  $\nu$  and  $\delta$  in Table II stand for the stretching and bending modes, respectively. Figure 9 shows the attributions of the associated symbols to specific species.

The experimentally observed IR band at  $660 \text{ cm}^{-1}$  is only compatible with the C1–H47 strong stretching LVM at  $644 \text{ cm}^{-1}$  in model C, as expected. The other low frequency modes ( $<715 \text{ cm}^{-1}$ ) in the other models are all bending modes with small oscillator strengths, which are not compatible with the experiment. The other LVMs associated with the C1–H47 bond in model C appeared at 1270, 1289, 1340, 1362, and  $1517 \text{ cm}^{-1}$ . These are overlaid on the LVMs of hydrogen terminating the peripheral carbon atoms. The experimentally observed IR bands are generally consistent with those in model C. The actual atomic configurations realized in the experiment should show wide structural variations in the HNG sample, including point defects, different sizes of

crystallites, and different structural correlations between the neighboring layers, which would broaden the LVM peak at  $644 \text{ cm}^{-1}$ , as experimentally observed.

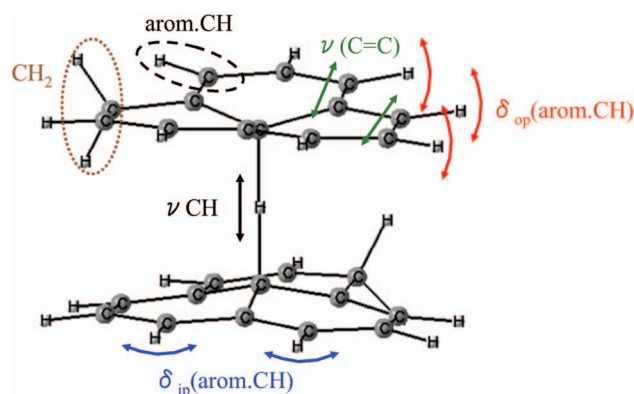


FIG. 9. (Color) Schematic representation for the symbols corresponding to the calculated IR active modes in Table II.

### C. Effect of Fe contamination

It was reported that the HNG powder contained a considerable amount of iron in the form of fine iron carbide particles,<sup>24,25</sup> incorporated from the steel balls and mortar used in the mechanical milling. This iron contamination significantly affects hydrogen storage; the broad low temperature peak and sharp high temperature peak vanished when the sample was prepared in the same hydrogen atmosphere using agate balls and mortar.<sup>23</sup> The present authors' group showed that the iron carbide fine particles actually store hydrogen, the results of which suggest a new hydrogen detection technique in steel.<sup>5,6</sup> We cannot exclude the possibility that the incorporated iron plays an important role in stabilizing the hydrogen trapped between layers, which is responsible for the low temperature TDS peak, because the model C is actually a metastable configuration and is not likely realized without some self-stabilizing factor.

### VI. SUMMARY AND CONCLUSIONS

This study revisits the still controversial hydrogen trapping state, corresponding to the low temperature peak in TDS, in HNG prepared by mechanical milling under a hydrogen atmosphere. The results can be summarized as follows:

- (1) The FT-IR spectrum of HNG exhibited a new broadband around 660 cm<sup>-1</sup>. This band disappeared by annealing at temperatures higher than 800 K.
- (2) Electron diffraction analysis detected an unusual contraction of the graphene interlayer distance in the hydrogenated sample. This recovered to a normal value by hydrogen desorption by annealing at temperatures higher than 800 K.
- (3) The  $\pi$ - $\pi^*$  plasmon peak of HNG was shifted to a higher energy side than that expected from a fragmented and defective structure.

All these results can be consistently explained by assuming that hydrogen atoms are trapped between the graphene layers, as suggested by our previous study of this material. The theoretical model calculations found the corresponding atom configuration, which is in reasonable agreement with the present and previous experimental results, except for the C-H bond length observed by neutron diffraction. This can be attributed to the small cluster size of the model structure. We would like to stress here that the present hydrogen trapping state is completely different from hydrogen physisorbed on a graphene surface found in CNTs and other graphite derivatives.<sup>26</sup> The present H-trapping model between the

graphene layers would be a kind of projection of the reality onto a graphite-hydrogen system. We do not exclude the possibility that other factors could play a role in stabilizing the structure, such as point defects within the graphene sheets, buckled and turbostratic graphene structure, and iron contamination.

### ACKNOWLEDGMENTS

The present work is partly supported by a Grant-in-Aid for Scientific Research of MEXT, Japan [Kibankenkyu A: 17206063; Tokutei-kenkyu (Priority Area): 474, "Atomic Scale Modification"].

- <sup>1</sup>S. Hynek, W. Fuller, and J. Bentley, *Int. J. Hydrogen Energy* **22**, 601 (1997).
- <sup>2</sup>A. C. Dillon, K. M. Jones, T. A. Bekkedahl, C. H. Kiang, D. S. Bethune, and M. J. Heben, *Nature (London)* **386**, 377 (1997).
- <sup>3</sup>M. Hirscher, M. Becher, M. Haluska, F. von Zeppelin, X. Chen, U. Dettlaff-Weglikowska, and S. Roth, *J. Alloys Compd.* **356–357**, 433 (2003).
- <sup>4</sup>S. Orimo, G. Majer, T. Fukunaga, A. Zuttel, L. Schlapbach, and H. Fujii, *Appl. Phys. Lett.* **75**, 3093 (1999).
- <sup>5</sup>S. Muto, T. Kimura, T. Tanabe, T. Kiyobayashi, and T. Maruyama, *Jpn. J. Appl. Phys.* **44**, 2061 (2005); T. Kimura, S. Muto, K. Tatsumi, T. Tanabe, and T. Kiyobayashi, *J. Alloys Compd.* **413**, 150 (2006).
- <sup>6</sup>K. Tatsumi, S. Muto, and T. Yoshida, *J. Appl. Phys.* **101**, 023523 (2007).
- <sup>7</sup>M. J. Frisch, G. W. Trucks, H. B. Schlegel *et al.*, GAUSSIAN 03, Gaussian Inc., Wallingford, CT, 2000.
- <sup>8</sup>C. H. R. Møller and M. S. Plesset, *Phys. Rev.* **46**, 618 (1934).
- <sup>9</sup>R. Krishnan, J. S. Binkley, R. Seeger, and J. A. Pople, *J. Chem. Phys.* **72**, 650 (1980).
- <sup>10</sup>D. M. Whitfield, D. Lamba, T. H. Tang, and I. G. Csizmadia, *Carbohydr. Res.* **286**, 17 (1996).
- <sup>11</sup>D. R. Gauger and W. Pohle, *J. Mol. Struct.* **744–747**, 211 (2005).
- <sup>12</sup>M. Veres, M. Koós, and I. Pócsik, *Diamond Relat. Mater.* **11**, 1112 (2002).
- <sup>13</sup>S. Xuguang, *Spectrochim. Acta, Part A* **62**, 559 (2005).
- <sup>14</sup>T. Heitz, B. Drévillon, C. Godet, and J. E. Bourée, *Phys. Rev. B* **58**, 13957 (1998).
- <sup>15</sup>H. Atsumi and K. Tauchi, *J. Alloys Compd.* **356–357**, 705 (2003).
- <sup>16</sup>S. Muto and T. Tanabe, *Philos. Mag. A* **76**, 679 (1997).
- <sup>17</sup>L. Laffont, M. Monthieux, and V. Serin, *Carbon* **40**, 767 (2002).
- <sup>18</sup>R. F. Egerton, *Electron Energy-Loss Spectroscopy in the Electron Microscope*, 2nd ed. (Plenum, New York, 1996).
- <sup>19</sup>W. A. Dinō, Y. Miura, H. Nakanishi, H. Kasai, and T. Sugimoto, *J. Phys. Soc. Jpn.* **72**, 1867 (2003).
- <sup>20</sup>A. Harada, F. Shimojo, and K. Hoshino, *J. Phys. Soc. Jpn.* **74**, 2270 (2005).
- <sup>21</sup>T. Fukunaga, K. Itoh, S. Orimo, M. Aoki, and H. Fujii, *J. Alloys Compd.* **327**, 224 (2001).
- <sup>22</sup>R. S. Mulliken, *J. Chem. Phys.* **23**, 1841 (1955).
- <sup>23</sup>M. D. Halls, J. Velkovski, and H. B. Schlegel, *Theor. Chem. Acc.* **105**, 413 (2001).
- <sup>24</sup>T. Kiyobayashi, K. Komiyama, N. Takeichi, H. Tanaka, H. Senoh, H. T. Takeshita, and N. Kuriyama, *Mater. Sci. Eng., B* **108**, 134 (2004).
- <sup>25</sup>T. Ichikawa, D. M. Chen, S. Isobe, E. Gomibuchi, and H. Fujii, *Mater. Sci. Eng., B* **108**, 138 (2004).
- <sup>26</sup>P. Bénard and R. Chahine, *Scr. Mater.* **56**, 803 (2007).